Earth and Space Science

RESEARCH ARTICLE
10.1029/2019EA000658

Global Bathymetry and Topography at 15 Arc Sec: SRTM15+

B. Tozer[1], D. T. Sandwell[1], W. H. F. Smith[2], C. Olson[1], J. R. Beale[3], and P. Wessel[4]

[1]Scripps Institute of Oceanography, La Jolla, CA, USA, [2]Laboratory for Satellite Altimetry, National Oceanic and Atmospheric Administration (NOAA), College Park, MD, USA, [3]National Geospatial-Intelligence Agency, Springfield, Virginia, USA, [4]School of Ocean and Earth Science and Technology, University of Hawaii at Manoa, Honolulu, HI, USA

Key Points:
- An updated global elevation grid is presented using a spatial sampling interval of 15 arc sec
- New bathymetry data include more than 33.6 million ship soundings and more than 6 years of non-repeat altimetry measurements
- The percentage of seafloor mapped by echo soundings remains low; our current compilation covers only 10.84% at 15-arc sec resolution

Supporting Information:
- Supporting Information S1

Correspondence to:
B. Tozer,
btozer@ucsd.edu

Citation:
Tozer, B, Sandwell, D. T., Smith, W. H. F., Olson, C., Beale, J. R., & Wessel, P. (2019). Global bathymetry and topography at 15 arc sec: SRTM15+. *Earth and Space Science*. *6*. https://doi.org/10.1029/2019EA000658

Received 5 APR 2019
Accepted 3 AUG 2019
Accepted article online 8 AUG 2019

Abstract An updated global bathymetry and topography grid is presented using a spatial sampling interval of 15 arc sec. The bathymetry is produced using a combination of shipboard soundings and depths predicted using satellite altimetry. New data consists of >33.6 million multibeam and singlebeam measurements collated by several institutions, namely, the National Geospatial-Intelligence Agency, Japan Agency for Marine-Earth Science and Technology, Geoscience Australia, Center for Coastal and Ocean Mapping, and Scripps Institution of Oceanography. New altimetry data consists of 48, 14, and 12 months of retracked range measurements from Cryosat-2, SARAL/AltiKa, and Jason-2, respectively. With respect to SRTM15_PLUS (Olson et al., 2016), the inclusion of these new data results in a ~1.4-km improvement in the minimum wavelength recovered for sea surface free-air gravity anomalies, a small increase in the accuracy of altimetrically derived predicted depths, and a 1.24% increase, from 9.60% to 10.84%, in the total area of ocean floor that is constrained by shipboard soundings at 15-arc sec resolution. Bathymetric grid cells constrained by satellite altimetry have estimated uncertainties of ±150 m in the deep oceans and ±180 m between coastlines and the continental rise. Onshore, topography data are sourced from previously published digital elevation models, predominately SRTM-CGIAR V4.1 between 60°N and 60°S. ArcticDEM is used above 60°N, while Reference Elevation Model of Antarctica is used below 62°S. Auxiliary grids illustrating shipboard data coverage, marine free-air gravity anomalies, and vertical gradient gradients are also provided in common data formats.

1. Introduction

The seafloor is a fundamental feature of our planet, with the oceans accounting for ~71% of Earths surface area (e.g., Ronov, 1994). Only ~15%, however, has been mapped at fine spatial resolution (≤800 m) using shipboard sounding methods (Wölfl et al., 2019). As such, its surface remains more poorly understood than that of many other planets (e.g., Ford & Pettengill, 1992; Smith et al., 1999), moons, and asteroids (e.g., Smith et al., 1997; Willner et al., 2014). This lack of knowledge is unfortunate given that seafloor bathymetry is of fundamental importance in many aspects of earth and biological sciences. For example, variations in bathymetry affect ocean circulation and mixing (e.g., Gille, 1994; Morrow et al., 1992; Sandwell & Zhang, 1989), which in turn moderate Earth's climate (e.g., Kunze & Llewellyn Smith, 2004; Munk & Wunsch, 1998). Such variations also influence local biodiversity and food resource potential (e.g., Koslow, 1997; Pitcher et al., 2008). Similarly, ocean volume influences geochemical budgets (e.g., Charette & Smith, 2010) and is important in climate modeling due to, for example, the oceans capacity to store heat and carbon (e.g., Stocker, 2013). The mapping of seafloor features and fabrics has also been fundamental in the discovery and advancement of plate tectonic theory (e.g., Haxby et al., 1983; Hess, 1962; Sandwell & Smith, 1997; Sclater et al., 1971), revealing the geologic history and activity of the ocean basins (e.g., Hochmuth et al., 2015; Matthews et al., 2011; Müller et al., 1997; Royer & Sandwell, 1989) and areas that may generate earthquakes and tsunamis (e.g., Mofjeld et al., 2004). Moreover, knowledge of the ocean floor is important for many practical applications, such as tsunami propagation modeling (e.g., An et al., 2014; Sepúlveda et al., 2018), infrastructure engineering, and scientific cruise planning (e.g., Smith, 1998).

For these reasons, among others, vast efforts have been made to map Earth's seafloor throughout the "technological revolution" of the past ~100 years (see Table 1). A major breakthrough occurred in the mid-1990s with the proliferation of satellite altimetry data collected by Geosat and ERS-1 spacecraft during their geodetic mapping phase. In lieu of adequate spatial coverage from shipboard data, Smith and

Earth and Space Science

10.1029/2019EA000658

Table 1
Selected List of Global (or Near Global) Bathymetric Grid Compilations

Date published	Map title	Author	Resolution (shipboard)	Resolution (satellite)	Satellite altimetry version	Construction style
1903	GEBCO First Edition aka the Monaco Chart	—	Tens of kilometers	—	—	Hand draw: contours
1910–1973	GEBCO Second–Fourth Editions	—	Tens of kilometers	—	—	Hand draw: contours
1976	The Floor of the Oceans	Heezen and Tharp	Tens of kilometers	—	—	Hand drawn: physiographic diagram
1977	World Ocean Floor	Heezen and Tharp	Tens of kilometers	—	—	Hand drawn: physiographic diagram
1981	World Ocean Floor	Cartographic Division, National Geographic Society	Tens of kilometers	—	—	Hand drawn: physiographic diagram
1973–1982	GEBCO Fifth Edition	Canadian Hydrographic Service	Tens of kilometers	—	—	Hand drawn: contours
1988	Digital Bathymetric Data Base 5 minute/ETOPO5	U.S. Naval Oceanographic Office	5 arc min	—	—	Digital grid: computer interpolation
1994	Predicted Bathymetry	Smith and Sandwell	2 arc min	9.9 km	V5.2	Digital grid: computer interpolation
1997	Predicted Bathymetry	Smith and Sandwell	2 arc min	9.9 km	V7.2	Digital grid: computer interpolation
1994-2003	GEBCO Digital Atlas (GDA)	British Oceanographic Data Centre	1 arc min	—	—	Digital vector: Digitized contours
2006	ETOPO2	World Data Service for Geophysics, Boulder	2 arc min	9.9 km	V8.2	Digital grid: Computer interpolation
2008	SRTM30_PLUS	Becker et al.	30 arc sec	8.9 km	V11.1	Digital grid: computer interpolation
2009	GEBCO_08	GEBCO 2008	1 arc min	8.9 km	V11.1	Digital grid: computer interpolation
2009	ETOPO1	World Data Service for Geophysics, Boulder	1 arc min	9.9 km	V8.2	Digital grid: computer interpolation
2014	SRTM15_PLUS	Olsen et al.	15 arc sec	8.9 km	V24.1	Digital grid: computer interpolation
2015	GEBCO_2014	Weatherall et al.	30 arc sec	8.9 km	V11.1	Digital grid: computer interpolation
2019	GEBCO_2019	GEBCO Bathymetric Compilation Group (2019)	15 arc sec	8.9 km	V24.1	Digital grid: computer interpolation
2019	SRTM15+V2.0	Tozer et al.,	15 arc sec	5.9 km	V27.1	Digital grid: computer interpolation

Note. This list is not exhaustive. Some grids include onshore topography, while others contain bathymetry only. Satellite altimetry version refers to the predicted depth grids, the version names are sequential from V1 (first) to V27 (current), and the suffix refers to the grid resolution in arc minutes. Note the satellite resolution column refers to the length scale of the Wiener filter used to stabilize the downward continuation of sea surface gravity anomalies to the regional seafloor depth (see section 3.1). The shipboard resolution for grids up to and including the GEBCO fifth edition are estimates only.

Table 2
Data Sources for Bathymetric Soundings (Multibeam and Singlebeam) Used to Construct SRTM15+V2.0

Data source	Area (V1) % 15 arc sec	Area (V2.0) % 15 arc sec	Area (V2.0) % 30 arc sec	% edited
NGDC_UNOLS	4.4000	4.3836	7.3458	4.91
JAMSTEC	1.5226	1.6883	2.1694	4.30
NGDC_GEODAS	1.0400	1.0334	2.5172	11.06
SIO_MISC	0.9577	0.9972	1.5489	13.12
NGA	0.0609	0.8998	1.4448	4.46
AGSO	0.3527	0.5538	0.7065	1.96
IBCAO	0.2051	0.2049	0.7776	0.03
GEOMAR	0.1776	0.1776	0.1818	0.06
GEBCO_IHO	0.1768	0.1767	0.2301	0.17
CCOM	0.1537	0.1666	0.2094	0.08
NOAA_US	0.1470	0.1464	0.1998	0.49
NGA_DNC	0.1345	0.1344	0.4894	1.23
IFREMER	0.1082	0.1077	0.1974	10.62
LAKES	0.0749	0.0749	0.1492	0.00
3DGBR	0.0920	0.0918	0.1123	11.36
NAVOCEANO	0.0087	0.0087	0.0099	0.06
TOTAL	9.6124	10.8457	18.2897	

Note. Percent edited refers to the percentage of data removed from each data set by human editors.

Sandwell (1994)—building on previous works from authors such as Dixon et al. (1983) and Haxby et al. (1983)—developed a method for transforming sea surface slope measurements acquired by the satellite altimeters into predictions of seafloor bathymetry. This enabled the creation of the first bathymetry grids with near-uniform spatial resolution (~15 km) and universal spatial coverage between latitudes ±72°. During the following decades, processing refinements and the inclusion of data from new altimeters have resulted in incremental improvements in the accuracy, resolution, and latitude range of these predictions. In particular, there have been two fundamental improvements to the original processing "recipe" for altimetric data. The first was the integration of global shipboard sounding compilations, which are used to calibrate the predicted depths (Smith & Sandwell, 1994) and as ground-truthed "pins" (e.g., Becker et al., 2009; Smith & Sandwell, 1997) to provide high-resolution mapping where available. The second was the development of custom waveform picking algorithms, tuned for optimal sea surface slope recovery (e.g., Garcia et al., 2014; Sandwell & Smith, 2005, 2009; Zhang & Sandwell, 2017; Zhang et al., 2018).

In this paper, we present SRTM15+V2.0—an updated global elevation grid at a spatial sampling interval of 15 arc sec (~500 × 500 m pixel size at the equator). This represents the newest iteration of the SRTM+ digital elevation model (DEM), constructed using our latest compilation of shipboard soundings and satellite-derived predicted depths. This follows from SRTM30_PLUS (Becker et al., 2009) and SRTM15_PLUS (V1; Olson et al., 2016), where the "plus" represents the addition of the ocean bathymetry, our principal contribution to the model. Motivation for this update stems from the improvement in both accuracy and resolution achievable by including a wealth of new data that has been acquired over the past few years, in addition to the inclusion of a previously underutilized global shipboard sounding compilation. Currently, there are three satellite altimeters in nonrepeat orbits from which we source data (see Table 3), and these have collected a substantial volume of new data over the past ~4 years; data from AltiKa, which operates using the Ka-band, are of particular importance due to its superior range precision (e.g., Smith, 2015; Zhang & Sandwell, 2017). In addition, the National Geospatial-Intelligence Agency (Figure 1) has provided a global shipboard sounding data set, which uniquely fills ~18.8 million grid cells at 15-arc sec resolution. These data are further bolstered by data from the Japan Agency for Marine-Earth Science and Technology (JAMSTEC) and three regional-scale high-resolution multibeam surveys that together provide an additional ~14.8

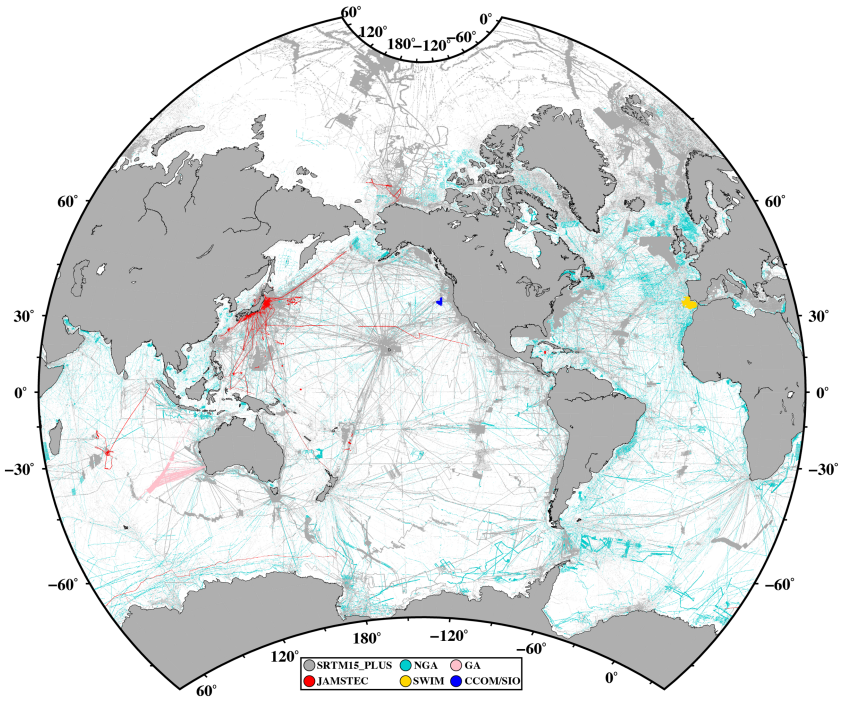

Figure 1. Global data coverage map of shipboard soundings included in SRTM15+V2.0 plotted to 89°N using a van der Grinten projection for visualization purposes. Readers are referred to the 15-arc sec source identification grid provided in Supporting Information S1 for a more accurate representation of the data coverage. Gray = SRTM15_PLUS (i.e., previous soundings). Colors = new soundings included in SRTM15+V2.0; cyan = National Geospatial-Intelligence Agency (NGA); red = Japan Agency for Marine-Earth Science and Technology (JAMSTEC); pink = Geoscience Australia (GA); yellow = South West Iberian Margin (SWIM); and blue = Mendocino composite cruises collected by Center for Coastal and Ocean Mapping (CCOM) and Scripps Institution of Oceanography (SIO). Note that above 80°N, the IBCAO v3 grid is used (Jakobsson et al., 2012).

million soundings. Collectively, SRTM15+V2.0 incorporates >33.6 million new ship-constained grid cells and greater than six cumulative years of altimetry measurements relative to SRTM15_PLUS (Olson et al., 2016). Onshore elevations are also updated and are greatly improved in the high and low latitudes, owing to the inclusions of the recently released ArcticDEM (Porter et al., 2018) and Reference Elevation Model of Antarctica (REMA; Howat et al., 2018) models, respectively (see Table 4).

2. Data Sources

2.1. Shipboard Sounding Database

As outlined in Table 2, SRTM15+V2.0 is constrained using a database of shipboard soundings that sample 10.84% of the ocean floor at 15-arc sec resolution (equal to 18.29% when sampled at 30 arc sec). This database has been compiled and maintained at Scripps Institution of Oceanography (SIO) over the past 20 years and consists of ~351 million unique sounding records (when median filtered at 15 arc sec) sourced from a variety of institutions. It is interesting to note that at 15-arc sec resolution, 29.7% of the grid cells containing sounding data have been sampled two or more times. This duplication is partly due to areas actually being surveyed more than once and partly due to the fact that there is significant repetition within the source data sets (as listed in Table 2). Much of the duplication occurs near the ports of the major oceanographic institutions as well as along the great circle tracks between institutions.

Many of these data are acquired as “cleaned” products from the source institutions and, to the best of our knowledge, have been sound velocity corrected. However, a variety of additional quality control and data editing steps has been applied. This includes the manual flagging of data that are obviously erroneous (percent edited in Table 2), as well as the decimation of data that are provided at resolutions higher than 15 arc sec. For details regarding these editing steps and for descriptions of many of the institutional source data sets, see Becker et al. (2009). Below, we briefly outline the new shipboard sounding data sets that have been added to our database since the release of SRTM15_PLUS and are included in the construction of SRTM15+V2.0.

2.1.1. National Geospatial-Intelligence Agency

The most significant contribution of new shipboard-derived bathymetry data included in SRTM15+V2.0 is a global compilation of single and multibeam soundings complied by the National Geospatial-Intelligence Agency. Prior to integration with SRTM15+V2.0, these data were decimated to 15-arc sec resolution and masked such that only points greater than ~2.3 km from a previous sounding were retained. This mask was applied to remove duplicates already included in our database and to preemptively avoid introducing artificial "steps" in the deep oceans, where experience has shown that two proximal, but independently collected, single beam soundings can have appreciable depth discrepancies. Post masking, ~18.8 million new soundings, distributed globally, remained, and these constrain many previously unmapped deep ocean regions (cyan in Figure 1). Unfortunately, metadata associated with these data are not available publicly, so we are not aware of the original acquisition dates or parameters.

2.1.2. JAMSTEC

SRTM15+V2.0 includes all publicly available processed bathymetry data collected by JAMSTEC (2016) vessels up until 1 January 2016 (Figure 1). New data included in our database consist of all cruises conducted post August 2012. These data represent an ~25% increase in the total volume of JAMSTEC data and are predominately located off the east coast of Japan (Figure 1).

2.1.3. Geoscience Australia—MH370 Search Region

As part of the search for missing Malaysia Airlines Flight 370 (MH370), the Governments of Australia, Malaysia and the People's Republic of China (2017) acquired ~279,000 km^2 of multibeam bathymetry data in the southeast Indian ocean (Figure 1). Prior to this surveying, the seafloor in this region was constrained almost entirely by predicted bathymetry (Smith & Marks, 2014). These data therefore fill a large gap and provide a rich insight into seafloor morphology in a previously uncharted region (e.g., Picard et al., 2018).

2.1.4. South West Iberian Margin

The South West Iberian Margin data set covers a cumulative area of ~183,000 km^2 (Figure 1) and incorporates data from 19 cruise legs. These consist of predominantly high-resolution multibeam data acquired between 2000 and 2006, gridded at 100-m resolution (Zitellini et al., 2009).

2.1.5. CCOM and SIO—Mendocino Compilation

Three recent cruises to a section of the Mendocino fracture zone (Figure 1) have collectively produced an ~55,500 km^2 grid of high-resolution multibeam data. These data were acquired by the Center for Coastal and Ocean Mapping (CCOM; Armstrong & Masetti, 2014) and Scripps Institution of Oceanography (SIO) in 2017/2018.

2.2. Satellite-Derived Marine Free-Air Gravity Anomalies

The marine gravity field derived from satellite altimetry is used to construct the base map for the global bathymetry as discussed below in section 3.1.1. The accuracy and resolution of the marine gravity depends primarily on the data coverage (track spacing) as well as the range precision of each altimeter (Garcia et al., 2014). To date, there have been seven satellite altimeters from which data are available and have (at least during some part of their lifetime) operated in a nonrepeat orbital phase that is useful for gravity field recovery (see Table 3).

Three significant previous releases of global bathymetry were those of Smith and Sandwell (1997; S&S97), Becker et al. (2009; SRTM30_PLUS), and Olson et al. (2014; SRTM15_PLUS (V1)). These models were released using predicted bathymetry generated using three versions of the marine gravity model (V7, V11, and V24) which had significant improvements owing to increases in altimetry data volume and accuracy (Table 1 and Figure 2).

Each of these models also had successor versions released subsequent to their original publication, as new data became available and ingested into each model. The final version of the S&S97 grid was released at 1-arc min resolution and used predicted bathymetry based on gravity model V18, which included data from Geosat and ERS-1 (Figure 2c). The final versions of the SRTM30_PLUS and SRTM15_PLUS (V1) models were based on gravity model V24 which also included 3 years of CryoSat-2 data and 14 months of data from the mapping phase of Jason-1. Gravity model V27 (used in SRTM15+V2.0) includes an additional 4 years of CryoSat-2 data, 12 months of Jason-2 data, and 14 months of AltiKa data.

The improvements in accuracy and resolution of the gravity model are documented in Figure 2. As can be seen in Figure 2b, the coherence in V27 has improved for all wavelengths between 40 and 12 km, and the minimum statistically significant wavelength (coherence $\geq$ 0.25; Bendat & Piersol, 2010) has improved from

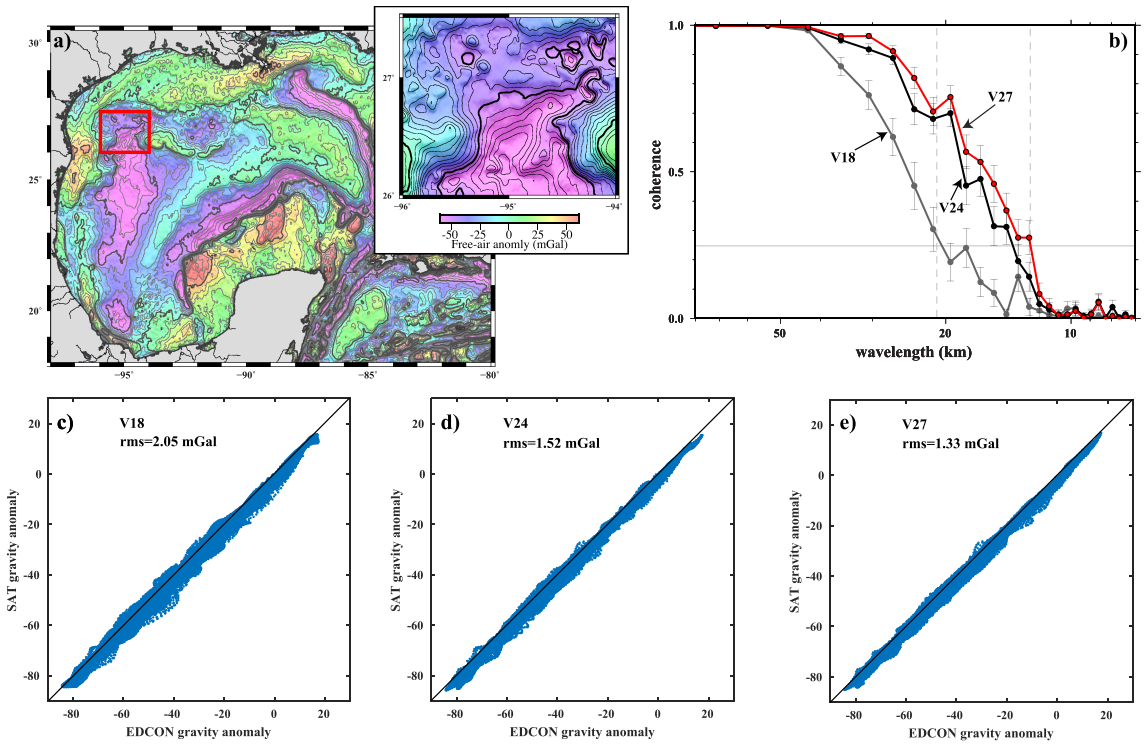

Figure 2. (a) Assessment of the accuracy and resolution of the marine gravity field based on gravity measurements provided by EDCON-PRJ Incorporated having a root-mean-square (RMS) accuracy of 0.5 mGal (Sandwell et al., 2013). The red box shows the inset map location used to calculate the coherence values shown in (b). The RMS accuracy of the satellite-derived gravity (SAT) has improved from 2.05 mGal for V18 to 1.33 mGal for V27 (c–e). The half wavelength resolution has improved from 11.5 km for V18 to 6.25 km for V27 (gray dashed lines). These improvements in accuracy and resolution map directly into improvements in the accuracy and resolution of predicted depth.

~21.5 to ~12.5 km. Hence, the predicted spatial resolution has improved from ~11.25 to ~6.25 km (half wavelength) depending on water depth—that is, two narrow features may blur into one if they are closer than ~6.25 km apart. Note that three altimeters (Jason-2, CryoSat-2, and AltiKa) continue to acquire data, so the gravity improvements will continue, particularly as the significantly more precise AltiKa altimeter repeats its dense mapping.

2.3. Onshore Digital Elevation Models

The elevation data used to construct the onshore portion of SRTM15+V2.0 were sourced from previously published DEMs as outlined in Table 4. Processing applied to these data is discussed in section 3.2. The most significant improvements over SRTM15_PLUS (V1) are achieved in high latitudes (>60 N° and >60°S), owing to the inclusion of the newly published ArcticDEM (Porter et al., 2018) and REMA (Howat et al., 2018) models, respectively.

2.3.1. ArcticDEM

Above 60°N, land elevations are sourced from ArcticDEM (Porter et al., 2018). These elevations are sourced from stereo autocorrelation techniques using pairs of satellite images acquired by the DigitalGlobe constellation (www.digitalglobe.com). It is important to note that the optimal high-resolution (2.0 m) version of these data represents "first return" elevations such that, for example, vegetation canopy may be represented rather than true "bare earth" elevations. For our application, at 15 -arc sec resolution, however, these effects are acceptable, given the vast improvement in spatial coverage and accuracy with respect to the Advanced Spaceborne Thermal Emission and Reflection Radiometer (ASTER) model used in SRTM15_PLUS.

2.3.2. SRTM CGIAR-CSI V4.1

Shuttle Radar Topography Mission (SRTM) elevation data constitute the largest onshore data source in SRTM15+V2.0, spanning latitudes 60°N–56°S. This model was originally produced by National Aeronautics and Space Administration (NASA) using satellite radar interferometry (Farr et al., 2007). In SRTM15+V2.0, an updated version, produced by the Consortium for Spatial Information (CGIAR-CSI V4.1), is used

(Jarvis et al., 2008). This version fills previous data voids using interpolation techniques and auxiliary high-resolution DEMs.

2.3.3. ASTER Global Digital Elevation Map V2

Between the latitudes of 56° and 62°S, a data coverage gap exists between SRTM CGIAR-CSI V4.1 (section 2.3.2) and REMA (section 2.3.2) due to the southern and northern spatial limits of these DEMs, respectively. This latitude band contains only a small fraction of land, constituting a few subantarctic islands. Data from the ASTER GEM V2 grid (Tachikawa et al., 2011) are used here. ASTER was jointly produced by the Japanese Ministry of Economy, Trade, and Industry and NASA via correlation of stereoscopic image pairs between 83°N and 83°S.

2.3.4. REMA

Below 62°S, elevations are sourced from REMA (Howat et al., 2018). This model was produced in the same way as ArcticDEM (section 2.3.1), using stereo autocorrelation techniques on pairs of satellite images acquired by the DigitalGlobe constellation (www.digitalglobe.com) and is vertically registered to Cryosat-2 and ICESat altimetry data (Howat et al., 2018). Similarly to ArticDEM, REMA elevations are first returns. REMA covers ~98% of the Antarctica landmass, with the largest void occurring below 88°S (known as the "pole hole"). In SRTM15+V2.0, these voids are filled by interpolation during processing (see section 3.2).

3. Grid Construction

When constructing SRTM15+V2.0, the onshore and offshore sections were created separately and merged as the final processing step. Boundaries between land and water bodies were defined using the Global Self-consistent, Hierarchical, High-resolution Geography Database (GSHHG) Version 2.3.7 (Wessel & Smith, 1996). At higher-resolution local scale, this is known to be inaccurate in some regions (misaligned by up to a few hundred meters) but is deemed adequate at the 15-arc sec resolution used in SRTM15+V2.0. It should also be noted that in SRTM15+V2.0, grid nodes are defined using pixel registration. This differs from the gridline registration used in previous SRTM_PLUS releases (e.g., Becker et al., 2009; Olson et al., 2016).

With regard to mapping of Earth's surface elevation, the main contribution of SRTM15+V2.0 lies in the construction of the bathymetric portion of the grid, in particular, the derivation of predicted bathymetry from satellite altimetry. The onshore portion of the grid is simply a compilation of several source data sets, each of which has been carefully constructed by various authors (see Table 4 and section 2.3). In sections 3.1 and 3.2, we outline the recipes used in the construction of both the bathymetric and topographic portions of SRTM15+V2.0.

3.1. Bathymetry Recipe

The bathymetry is constructed in two main phases. The first phase is a 1-min construction using a combination of satellite gravity and ship soundings. The second phase takes this base map and increases the resolution to 15 arc sec where ship soundings are available. This is achieved using a remove-interpolate-restore approach (e.g., Becker et al., 2009). Here we briefly review these two phases and provide some intermediate results to highlight improvements with respect to previous publications.

3.1.1. Predicted Bathymetry to ±80° Latitude

The development of the predicted bathymetry follows the basic approach outlined by Smith and Sandwell (1994) and Smith and Sandwell (1997) with improvements in data quality that enable a prediction at shorter wavelengths. The processing steps are as follows:

1. Grid available bathymetric soundings on a 1-min Mercator grid between latitudes of ±81° using the Generic Mapping Tools (GMT) interpolation function *surface*, which uses continuous curvature splines in tension (Smith & Wessel, 1990). Here a tension factor of 0.6 is used. This deep-water grid is combined with the shallow areas of the GEBCO 1-min grid (GEBCO, 2003), based on hand-drawn contour maps, to form a complete global bathymetry/topography model. There is no satellite gravity information in this grid.
2. Separate the bathymetry grid into low-pass and high-pass components using a Gaussian filter (0.5 gain at 160-km full wavelength). This filtering and the downward continuation (Step 4) are performed with a multiple strip, 2-D Fast Fourier Transform (FFT) that spans 0–360° longitude to avoid Greenwich edge effects.
3. Form high-pass filtered gravity using the same Gaussian filter.
4. Downward continue the high-pass filtered gravity to the low-pass filtered bathymetry using Laplace's equation. A depth-dependent Wiener filter is used to stabilize the downward continuation. In the Smith

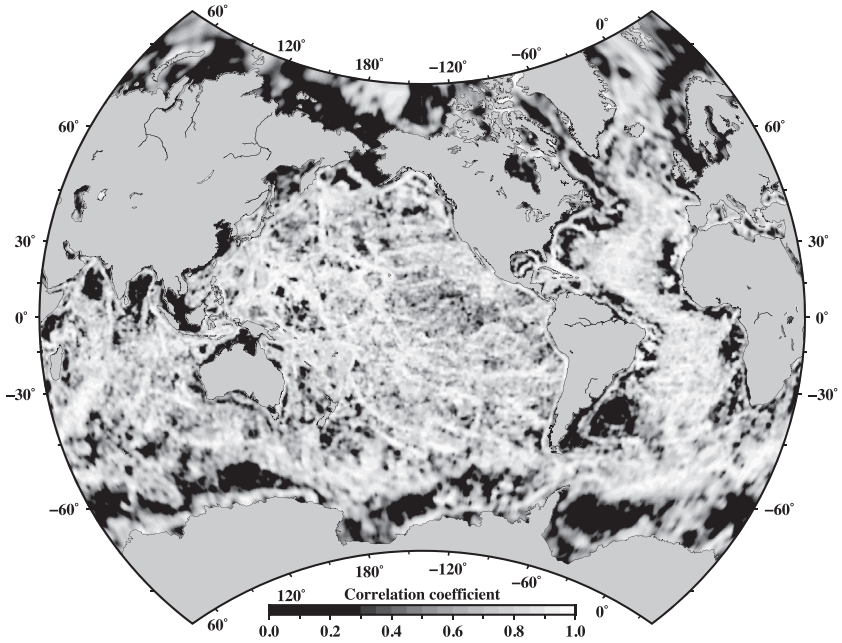

Figure 3. Correlation coefficient obtained by linear regression between topography and gravity over the 12- to 160-km wavelength band. Bathymetric prediction works well in areas of high correlation and poorly in areas of low correlation. Areas of low correlation are generally flat because of thick sediment cover. These include the old ocean basins, wide continental margins, and Arctic/Antarctic areas.

and Sandwell (1994) publication, the length scale of that filter was set to 9.9 km. That was reduced to 8.9 km for the predicted depths used in the SRTM30_PLUS (Becker et al., 2009) and SRTM15_PLUS (Olson et al., 2016) grids. The improvements in the gravity accuracy and resolution discussed above have enabled an additional reduction to 5.9 km which results in better resolution in the predicted depths.

5. Accumulate high-pass filtered soundings and corresponding downward-continued gravity into small overlapping areas (these are scaled with latitude to have search radii of ~160 km) and perform a robust regression analysis. The search radius is increased or decreased by a factor of $\sqrt{2}$ if the number of samples is less than or more than sampling thresholds of 42 and 170 points. A map of the linear correlation coefficient from this analysis is shown in Figure 3. In sediment-free areas, where the relief is much less than the mean ocean depth, the topography:gravity transfer function should be constant and equal to $(2\pi G\Delta\rho)^{-1}$ where $\Delta\rho$ is the crust to water density contrast (i.e., 13.25 m/mGal for a crustal density of 2,800 kg/m^3). After these operations, the ratio of topography to gravity is independent of wavelength, so in the space domain, a linear regression is appropriate. This works well where sediment cover is thin, such as young seafloor. However, in areas where the sediments are thick and the seafloor is flat, topography and gravity are poorly correlated ($\leq$0.3), so we assume the seafloor is flat and set the topography:gravity ratio to zero. Finally, there are intermediate cases where topographic depressions will be sediment filled while the highs protrude above the sediments, so the topography:gravity relationship is nonlinear. In these areas we estimate two topography-to-gravity slopes for positive and negative gravity, respectively. It is these partially sedimented areas that make the bathymetric problem difficult; continental margins and shelves pose similar problems.
6. Regional topography:gravity ratio estimates are gridded and multiplied by the high-pass filtered/downward-continued gravity to form high-pass filtered predicted bathymetry.
7. The total predicted bathymetry is given by summing the high-pass filtered predicted bathymetry from (6) and the low-pass filtered bathymetry from (2).
8. Finally, the pixels constrained by ship soundings or coastline data are reset to the measured values and a minimum curvature interpolation routine (similar to the method described in section 3.1.2) is used to perturb the surrounding predicted values toward the measured values (i.e., polishing). Coastline points from the GSHHG model (Wessel & Smith, 1996) provide the zero-depth estimates, and an ocean mask is used to remove any false islands by resetting these pixels to a depth of −10 m.

The final step (8) dramatically increases the accuracy and resolution of the bathymetric grid in well-surveyed areas. In addition to the 1-min bathymetry, a matching grid of source identification numbers (SID) is constructed to be used for determining the source of the depth information for each grid cell. The 1-min topography grid (Version 19) and matching gravity grid (Version 27) are provided as Supporting Information S1 and are available by anonymous ftp (topex.ucsd.edu).

3.1.2. Global Bathymetry at 15 Arc Sec: Remove-Interpolate-Restore

The second phase uses the 1-min near-global bathymetry grid (from section 3.1.1) along with the IBCAO Arctic grid v3 (Jakobsson et al., 2012) for latitudes greater than 80°N to form a complete map at 15 arc sec. This grid was generated via a remove-interpolate-restore approach using the following steps:

1. Depth values from the 1-min bathymetry and IBCAO v3 grids are first interpolated onto a pixel registered 15 arc sec grid using the GMT function *surface*. Here a tension factor of 0.35 was used (IHO-IOC Commission, 2018). This is done in six overlapping latitude bands to partially account for the changing longitude cell size with latitude.
2. *Remove:* The predicted depths are sampled at all colocated ship-constrained depths and removed from those values to produce "residual depths." This residual depth grid is then supplemented with zero depth values at grid cells ≥10 km from a real sounding. These additional zero data will prevent the interpolation algorithm from creating overshoots in voids that are adjacent to areas of sharp depth variation.
3. *Interpolate:* The residual/zero depth values are then interpolated at 15 arc sec using a cubic spline in tension with a tension value of 0.55 (selected based on experience), implemented by the GMT function *surface*. Again, this is done in six overlapping latitude bands.
4. *Restore:* The six interpolated residual depth grids from Step 3 are then added to their corresponding predicted-depth grids derived in Step 1. This step ensures the bathymetry will match the depth soundings at the full 15-arc sec resolution where available and blend smoothly into the bathymetry predicted from gravity.
5. Finally, the GMT function *grdblend* is used to combine these six grids into a single global grid with longitude range −180–180 having 86,400 pixels and the latitude range −90–90 having 43,200 pixels.

A matching SID grid is also constructed to be used for determining the source of the depth information for each grid cell (see section 5.1).

3.2. Topography Recipe

The processing steps used to combine the onshore DEMs used in SRTM15+V2.0 (as described in section 2.3) and merge these with our global seafloor bathymetry grid (section 3.1) were as follows:

1. Acquire DEMs from sources listed in Table 4.
2. Convert all DEMs to a common format (16-bit integer netCDF GMT grids) and, if required, convert the coordinates to geographic (longitude/latitude) and WGS84 datum. Conversions were performed using the GMT function *grdconvert*, and coordinate conversions were performed using the PROJ4 *cartographic coordinate system filter (CS2CS)* function.
3. Decimate each source DEM from their various source resolutions to 15 arc sec and pixel registration. This involved either filtering or regridding the data. For filtering, a Gaussian function defined by 6σ value (effectively the filter wavelength) of 1 km was applied using the GMT function *grdfilter*. For regridding, the raw data were written as XYZ text files, decimated to 15-arc sec resolution using the GMT function *blockmedian*, and finally regridded using the GMT function *surface* and tension factor of 0.55, chosen to produce reasonable results for areas with steep topography.
4. Ensure all elevations are referenced to the geoid (i.e., elevations are set as orthometric height in meters). Both ArcticDEM and REMA elevations are referenced relative to the WGS84 ellipsoid datum. Hence, the vertical difference between the geoid and ellipsoid, as defined by the EGM96 geoid model (Lemoine et al., 1997), was determined at each grid cell and subtracted from the original elevations. The GMT functions *grdsample* and *grdmath* were used to perform this operation.
5. Merge all DEMs using the GMT function *grdblend* to produce a single global grid of onshore elevations.
6. Clip the final grid along coastlines, as defined by the GSHHG model (Wessel & Smith, 1996). All nonland pixels were set as "NaN."

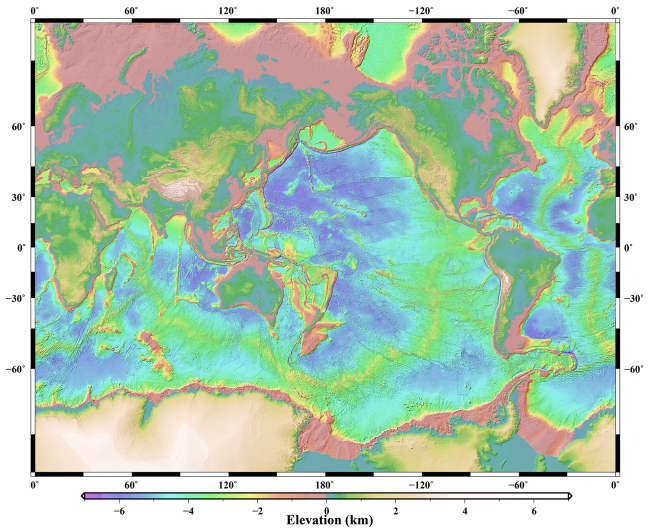

Figure 4. SRTM15+V2.0 at 15-arc sec resolution plotted to ±80° latitude using a Mercator projection.

The final processing step takes the global land grid and merges this with the global bathymetry grid. As the two grids align together at zero elevation along the GSHHG coastlines, merging was performed using the GMT function *grdmath*.

4. Results, Grid Assessment, and Discussion

4.1. SRTM15+V2.0

Figure 4 shows the SRTM15+V2.0 grid plotted between ±80°. This provides a significant improvement in both accuracy and resolution with respect to SRTM15_PLUS. Figure 5 shows the difference in elevations between SRTM15+V2.0 and SRTM15_PLUS (i.e., positive values are positive elevation changes relative to SRTM15_PLUS) and highlights areas of improvement. There are several features that stand out.

Onshore, in the high and low latitudes, there are very long-wavelength changes (e.g., negative in Greenland and positive/negative in eastern Antarctica) which result from the geoid correction applied in SRTM15+V2.0. Above 60°N, there is a prominent southwest-northeast strip pattern, which reflects the replacement of the ASTER Global Digital Elevation Map orbital pattern (used in SRTM15_PLUS) with ArcticDEM. Short wavelength changes, for example, near the coast of Antarctica and throughout Alaska, reflect the improved resolution of REMA and ArcticDEM, respectively. There is relatively less change in the ±60° band, where the SRTM DEM has not been extensively modified. However, in regions with large topographic gradients (e.g., the Himalaya, Andres, and Rockies) and between latitudes 38.25° and 50°S, variations are evident, and these reflect improved accuracy.

In the oceans, elevation changes can generally be categorized as one of four types. First, there are narrow linear strips, traceable over long distances with local changes sometimes exceeding ±200 m. These reflect the path of new multibeam transits, which have replaced predicted depths. Second, adjacent to these tracks, but much more commonly associated with new singlebeam tracks, are large (a few degrees), elongate "blobs"

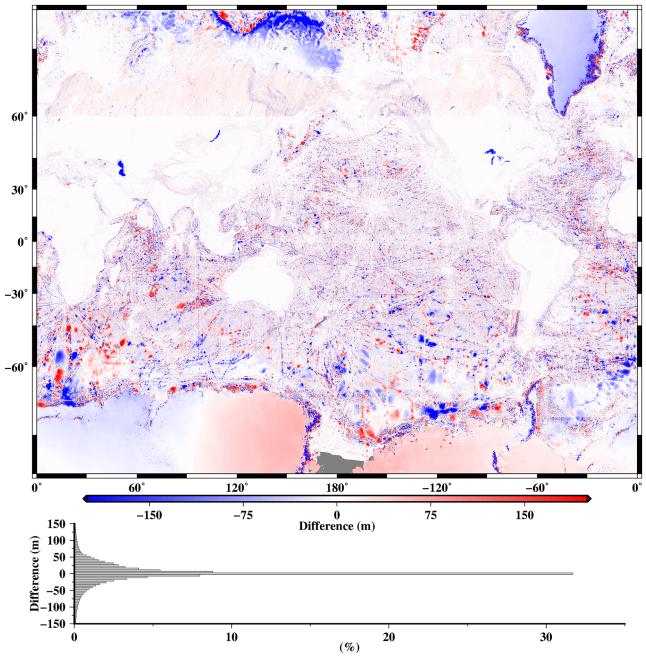

Figure 5. (Top) Map showing the elevation differences between SRTM15+V2.0 and SRTM15_PLUS in meters. Note that white regions (near zero difference) mirror the SRTM15_PLUS SID grid (i.e., preexisting sounding data). Gray shows regions that contained NaN values in SRTM15_PLUS (V1). (Bottom) Histogram showing the same distribution as depicted in the map.

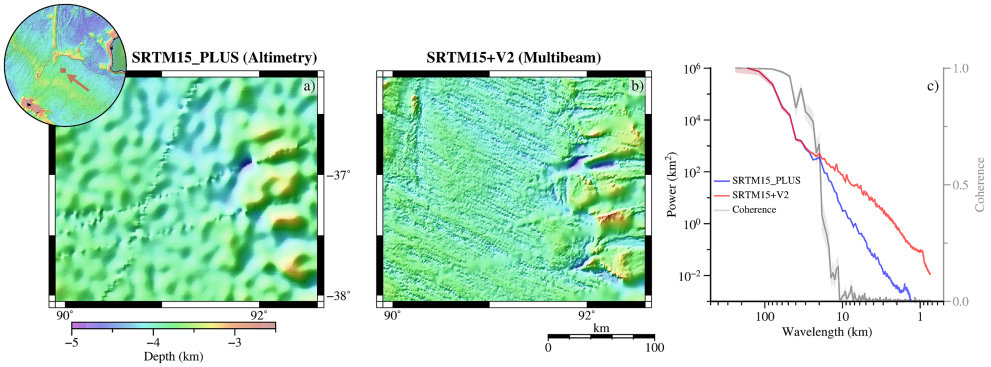

Figure 6. Comparison between (a) predominately satellite-derived predicted bathymetry from SRTM15_PLUS and (b) predominately multibeam bathymetry in the MH370 search area included in SRTM15+V2.0. The location of (a) and (b) is shown as red shading as indicated by the red arrow in the inset map. (c) Spectral analysis of (a) and (b) plotted as a function of wavelength. Blue and red curves are radial power spectra of (a) and (b), respectively (note 1σ values are plotted as transparent overlays and are only visible at wavelengths >50 km); gray curve is cross-spectral coherency (1σ plotted as transparent overlay).

of uniform polarity. These result from interpolation, when no other shipboard data occur in the vicinity of a local pull-up or push-down of seafloor along a ship track. Third, there are regions of local, high amplitude and short wavelength changes of both polarity. These occur in regions where new multibeam surveys have been included, for example, the MH370 search region Southwest of Australia. Finally, there is an apparent random background "orange peel" texture, of approximately ±75 m. This principally reflects the change in noise level of altimetrically predicted depths. Both the V2 and V1 predicted depths have some of this noise component, so this does not reflect the absolute improvement in predicted depths. Comparison of V1 and V2 predicted depths with our shipboard data shows the overall root-mean-squared (RMS) improvement is small, ~3 m; however, for short wavelength features, such as the peaks of conical seamounts, the predicted depths are much improved with absolute depth changes on the order of ~100 m observed (e.g., Figure S1).

4.1.1. Radial Power Spectra and Coherency

In order to better understand the improvements in spatial resolution achieved in SRTM15+V2.0, the radial power spectra of both SRTM15_PLUS and SRTM15+V2.0, in addition to their cross-spectral coherency, were calculated at several locations. Figures 6 and 7 show two examples, from the MH370 search area in the Southeast Indian Ocean (offshore) and the Concord Mountains of Victoria Land, Antarctica (onshore). In both of these locations, the spatial resolution has improved drastically owing to the inclusion of new multibeam and REMA imagery data, respectively.

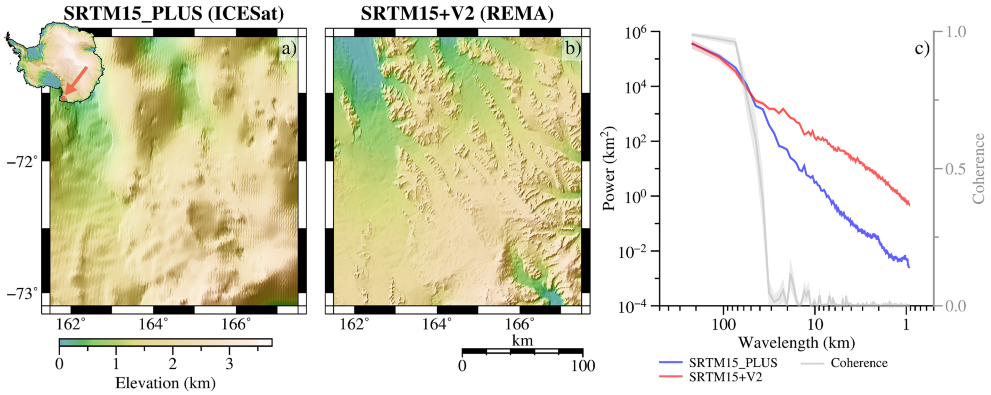

Figure 7. Comparison between (a) ICESat topography included in SRTM15_PLUS and (b) Reference Elevation Model of Antarctica (REMA) topography included in SRTM15+V2.0. The location of (a) and (b), centered on the Concord Mountains of Victoria Land, is shown as red shading in the inset map. (c) Spectral analysis of (a) and (b) plotted as a function of wavelength. Blue and red curves are radial power spectra of (a) and (b), respectively (note 1σ values are plotted as transparent overlays and are only visible at wavelengths >50 km); gray curve is cross-spectral coherency (1σ plotted as transparent overlay).

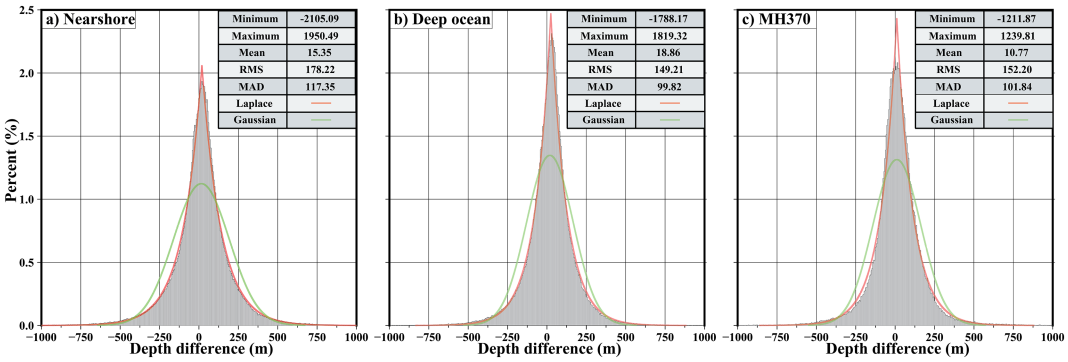

Figure 8. Histograms showing the depth differences calculated by comparing predicted depths with colocated shipboard soundings for (a) 25 globally distributed cruises located between coastlines and the continental rise, (b) 25 globally distributed cruises located in the deep oceans, and (c) the MH370 search region (Figure 1). Inset tables show statistics in meters. Red and green curves are best-fit Laplace and Gaussian distributions, respectively. RMS= root-mean-square error; MAD = mean absolute deviation.

In the Southeast Indian Ocean, Figure 6c shows the energy in the power spectra for both SRTM15_PLUS and SRTM15+V2.0 decreases steadily for wavelengths ≤20 km; however, the energy in V2.0 remains ~10–500 times greater, owing to the short wavelength information supplied by the new multibeam data. The coherency remains >0.5 at wavelengths ≥12 km and then drops to near zero. This demonstrates that the predicted depths in V1 sufficiently capture wavelengths greater than 12 km but no information at shorter wavelengths, owing to the 11.9-km cutoff used when filtering these data during the calculation of predicted depths (see section 3.1.1).

In Antarctica, Figure 7c shows a similar pattern to that described above. The coherency at wavelengths >40 km is high (>0.5); however, this drops off rapidly at shorter wavelengths. This occurs at the limit of spatial resolution in the ICESat data used in SRTM15_PLUS. The power spectra clearly show that the REMA data (red curve) used in V2.0 contain information down to the 15-arc sec (~500 m) resolution, consistent with visual inspection of the topography shown in Figures 7a and 7b.

4.2. Predicted Depth Uncertainties

In order to estimate the vertical uncertainties associated with altimetrically derived predicted depths, we used a subset of shipboard soundings and compared their depths with colocated predicted depths using our 1-arc min grids, prior to the "polishing" processing step (as described in section 3.1.1). If we assume the shipboard-derived depths as "ground-truth," it follows that the differences between these depth values provide an estimate of the uncertainties associated with the predictions. For this comparison, 50 unique cruises, 25 from the deep oceans and 25 located between coastlines and the continental rise ("near coast"), were selected. Figure 8 shows the results for the deep oceans, near coast, and MH370 search area. We find that bathymetric grid cells derived from satellite altimetry have estimated RMS uncertainties of ±150 m in the deep oceans and ±180 m near coasts. The larger uncertainty obtained near coasts is likely due to the higher frequency and larger amplitude depth variability in these regions with respect to the deep oceans.

For the MH370 search region, our uncertainty results match closely to those obtained by Picard et al. (2018), who have also analyzed these data and showed that 62% of the mapped seafloor was within ±100 m of the predicted depths from SRTM15_PLUS (Olson et al., 2016). As expected, the high-resolution multibeam data reveal many short wavelength features not recovered by predicted bathymetry (with a ~6-km spatial resolution), and hence, they report differences of greater than ±100 m for ~38% of the region, with a maximum difference of 1,900 m.

An important implication of Figure 8 is that when using these predicted depth data for modeling applications, such as tsunami propagation, a Laplacian distribution (as opposed to a Gaussian) is more representative of the error distribution. The Laplacian distribution holds true for most of the individual cruises; however, there is variation between cruises, with depth uncertainties from some cruises distributed randomly. A detailed investigation of these errors and their relationship with respect to, for example, geological environment is the subject of a concurrent study (Sepúlveda et al., 2019).

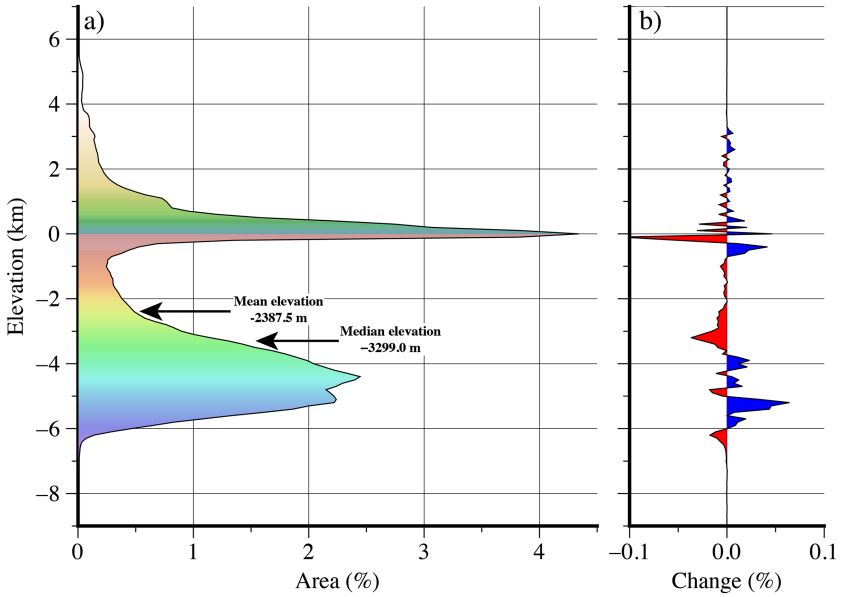

Figure 9. (a) Global hypsometry curve obtained from SRTM15+V2.0 using a 100-m bin interval. Note the color scale is the same as that used in Figure 4. (b) Change in area with respect to SRTM30_PLUS (Becker et al., 2009).

4.3. Global Hypsometry

Figure 9 shows the global hypsometric curve (distribution of area as a function of elevation) obtained from SRTM15+V2.0 using an elevation interval of 100 m. The most striking feature is the bimodal distribution of Earth's surface, which is well-known from previous studies (e.g., Sandwell & Smith, 2001; Smith & Sandwell, 1997; Weatherall et al., 2015). As is shown, a large portion (53.64%) of the Earth's surface is confined between depths of 3 and 6 km, and a secondary peak containing 30.56% falls between ±1.0 km.

Sandwell and Smith (2001) explained the two peaks seen in the deepest mode (at ~5,100- and ~4,250-m depth) in terms of the nature with which seafloor cools and subsides with age. The 5,100-m peak occurs due the flattening of sea floor near this depth, once it reaches an age of ~80 Ma (e.g., Parsons, 1982; Parsons & Sclater, 1977). Two processes may be responsible for the peak at 4,250 m. Smith and Sandwell (1997) showed that when seafloor area is plotted as a function of age, there is a peak at ~20–33 Ma, due to an increase in seafloor production at this time and following a plate cooling model (e.g., Parsons & Sclater, 1977), seafloor of this age currently resides around this depth (e.g., Müller et al., 2008). Crough (1978), on the other hand, showed that seafloor swells associated with midplate volcanoes, such as Hawaii and Cape Verde, uniformly reside at this depth, which also adds to this peak.

Smith and Sandwell (1997) further showed that, although plate cooling models fit the observed hypsometric curve well for depths up to ~5 km, the predictions and observations diverge at greater depths. This suggests that processes other than plate cooling must affect seafloor depth. That the seafloor does not uniformly

Table 3
Data Sources for Satellite Altimetry (Sea Surface Slope) Used to Construct SRTM15+V2.0

Altimeter	Cumulative months of data	New in SRTM15+V2.0	# measurements (20 Hz; 10^6)	Range precision (mm)	Latitude range (°)
Geosat	18	0	517	57.0	±72
ERS1	12	0	442	61.8	±81
Envisat	6	0	128	51.0	±81
Jason-1/2*	27	14	746	43.0	±66
CryoSat-2*	102	48	3,011	43.7	±88
AltiKa*	33	12	847	20.5	±81

*Altimeters that are currently active and collecting data in nonrepeat orbits.

Table 4
Onshore Digital Elevation Models Used to Construct SRTM15+V2.0

Data source	Latitude range	Surface area (km^2)	Reference
ArcticDEM R7	85–60°N	17,195,722	Porter et al. (2018)
SRTM CGIAR-CSI V4.1	60°N–56°S	116,914,000	Jarvis et al. (2008)
ASTER GDEM V2	56–62°S	1,569	Tachikawa et al. (2011)
REMA R1	62–90°S	13,694,743	Howat et al. (2018)

flatten out at the same age (Marty & Cazenave, 1989), as predicted by plate cooling models, provides further evidence for secondary processes. Smith and Sandwell (1997) were able to explain this discrepancy by invoking a stochastic reheating model in which the cooling, subsiding plates are affected by volcanism and thermal rejuvenation, such that they are uplifted by some amount and then continue to subside.

5. Auxiliary Data Products, Release Formats, and Visualization

Additional data products created as part of this study are listed in Table 5. These are included as supplementary material in various data formats (Table 6) and available online as Google Earth overlays (topex.ucsd.edu). For simple visualization of all data products using a digital globe, we recommend the readers to install the freely available GPlates software (Müller et al., 2018) and open the GPlates project file (.gproj) provided in Supporting Information S1.

5.1. Source Identification Grid and Table

The SID grid is used to distinguish between grid cells constrained by shipboard bathymetry and those that are sourced from altimetric predictions. Each grid cell that is constrained by a sounding contains a unique integer (SID) that is used as an index in our SID table. Currently, if a grid cell is constrained by more than one sounding, the mode is used as the SID. The SID table provides key information related to the unique cruise, namely, (1) the name of the data source file (see Table S1); (2) the nature of the data (public or private); (3) the source institution; and when available (4) provides a link to associated metadata. The SID table is provided as an ASCII text file in Supporting Information S1. An accompanying command line program that takes an SID index as standard input and returns the SID table information as standard output is also provided.

6. Future Outlook

Despite continued efforts to collect and collate shipboard sounding data, our latest compilation only samples 10.84% of the global ocean at 15-arc sec resolution, a value similar to that of the GEBCO_2014 catalog (e.g., Mayer et al., 2018; Weatherall et al., 2015). Acknowledging that the rate at which new seafloor is currently being mapped (and/or data are being made publicly available) remains unsatisfactorily low, a recent consortium have committed to the ambitious goal of compiling a global high-resolution (between 800 and 100 m) bathymetric database by 2030, as part of the Nippon Foundation—GEBCO Seabed 2030 Project (Mayer et al., 2018). Such an achievement would revolutionize our understanding of not only the seafloor but also many geological, biological, and climatic processes. The new data that are collected, in addition to

Table 5
Additional Data Products Supplied as Supplementary Material

Grid type	Grid resolution	Latitude range (°)	Unit
Elevation change (V2.0-V1.0)	15 arc sec	±90	m
Source identification grid (SID)	15 arc sec	±90	—
Marine Free-air gravity anomalies (V27.1)	1 arc min	±80	mGal
Marine vertical gravity gradient (V27.1)	1 arc min	±80	Eötvös
Gravity/topography linear correlation coefficient	2 arc min	±80	—

Table 6
List of Data Types Supplied for All Data Products

Format type	Data structure	File extension	SRTM15+V2.0 file size	FFA (V27) file size	VVG (V27) file size
GMT	32-bit int NetCDF*	.nc	2.70 Gb	0.42 Gb	0.80 Gb
GeoTIFF	TIFF raster	.tiff	3.40 Gb	0.49 Gb	0.90 Gb
Google Earth	KML	.kmz	0.46 Kb	9.3 Kb	8.6 Kb
GPlates	GPML	.gpml	16.0 Gb	14.00 Gb	0.90 Gb

Note. The GPML files are intrinsically linked to either a GeoTIFF or GMT NetCDF grid. FFA = Marine Free-air gravity anomalies; VGG = Marine vertical gravity gradient. *FFA and VGG NetCDFs are 32-bit float.

the privately held data that are made available via this project, will be highly complementary with satellite altimetry data. For one, while data gaps remain during the lifespan of the Seabed 2030 project, these data will help better constrain the gravity/topography transfer function (section 3.1.1) resulting in more accurate predicted depths. Moreover, the combination of independently derived shipboard bathymetry and satellite gravity data provides a useful means for investigating many tectonic questions, for example, the tectonic setting of seamount formation (e.g., Watts et al., 2006) and the isostatic compensation of seafloor features (e.g., Bansal et al., 2005). Many such studies may be stimulated by combining new shipboard bathymetry with altimetrically derived gravity anomalies. Altimetry will, therefore, remain an important method for ocean floor exploration (particularly in the deep ocean) for many years to come.

Fortunately, the future of altimetry, at least in the near term, appears promising. So long as AltiKa remains operational in its current drifting phase (e.g., Dibarboure et al., 2018), we anticipate the periodic inclusion of these data, along with those from the other operational altimeters (CryoSat-2, Jason-2, and Sentinel-3), will continue to provide valuable improvements in the accuracy of the marine gravity field and, hence, accuracy of predicted bathymetry. In the long term, NASA is planning to launch a new swath altimeter mission called the Surface Water and Ocean Topography Mission (SWOT) in 2021 (Fu et al., 2012). SWOT, with its smaller footprint and additional cross-track slope measurement, could improve the gravity accuracy by perhaps another factor of 5 and also improve spatial resolution on the shallow continental margins. The improved accuracy could reveal thousands of uncharted seamounts (Wessel, 2001) as well as the fabric of the abyssal hills in the deep ocean.

In terms of near-coast mapping, one recent advance comes from the Advanced Topographic Laser Altimeter System, which was recently launched on board ICESat-2 (Markus et al., 2017). Preliminary data have demonstrated that this instrument can recover ocean bottom returns in clear/nonturbid shallow water (e.g., Ramsayer, 2018). Although such returns are recovered only along sparse track lines, they provide a means of validating satellite imagery and airborne LIDAR images that also "see" the ocean bottom but lack an absolute elevation reference. Hence, collectively, these techniques can be combined to map large regions of shallow water, which may prove highly beneficial in mapping near-coastal regions at a fraction of the time and cost compared to using ships.

We therefore plan year-to-year releases of SRTM15+V2 using a decimal version control suffix (i.e., the next release in 2020 will be named SRTM15+V2.1). A move to version 3.0 will coincide with the next major improvement. Conceivably, this could be the inclusion of data collected by the SWOT mission.

7. Conclusions

1. We have created a new global elevation grid, using a spatial sampling interval of 15 arc sec. The spatial resolution is equal to the sampling interval on land and when ocean grid cells are constrained by shipboard soundings, while it is ~6 km (half wavelength) for cells constrained by satellite-derived predicted depths.
2. The percentage of seafloor that has been mapped using shipboard techniques (in the public domain) remains low. Our current compilation, although not exhaustive, covers only 10.84% at 15-arc sec resolution.
3. Altimetrically derived depths have RMS uncertainties of ±150 m in the deep oceans and ±180 m between coastlines and the continental rise.

4. The addition of future altimetry data (currently being acquired by three active satellites) will continue to provide valuable improvements in the accuracy and spatial resolution of the marine gravity field and, hence, predicted bathymetry.
5. Bathymetric prediction will remain a principle method by which ocean depth (particularly in the deep ocean) is determined for at least the next 10 years, until such time that holistic mapping by acoustic methods is accomplished.

Acknowledgments
A number of colleagues have made useful suggestions and we thank the three anonymous reviewers for their helpful comments that improved an earlier version of the manuscript. Particularly, we thank Ignacio Sepúlveda for helpful discussions related to the predicted bathymetry error distribution and Susheel Adusumilli for highlighting the potential of ICESat-2 for bathymetry recovery. Brook Tozer was supported by the Office of Naval Research (N00014-17-1-2866) and a Cecil and Ida Green Foundation scholarship. Additional research support was provided by the NASA SWOT program (NNX16AH64G). The Generic Mapping Tools (Wessel et al., 2013) were used extensively in data analysis and to generate all figures. This study benefits from data collected as part of the search for aircraft MH370; we wish to honor the memory of the 239 people who tragically lost their lives after boarding this flight. Our deepest sympathies go out to those who lost their loved ones. The manuscript contents are solely the work and findings of the authors and do not constitute a statement of policy, decision or position on behalf of NOAA or the U.S. Government. NGA approved for public release #19-486. All data sets generated during this study can been obtained following instructions provided in the supplementary material.

References

An, C., Sepúlveda, I., & Liu, P. L. (2014). Tsunami source and its validation of the 2014 Iquique, Chile, earthquake. *Geophysical Research Letters*, *41*, 3988–3994. https://doi.org/10.1002/2014GL060567

Armstrong, A. A., & Masetti, G. (2014). CRUISE REPORT RV Atlantis (AGOR-25) U.S. extended continental shelf cruise to map sections of the Mendocino Ridge. Durham, NH.

Bansal, A. R., Fairhead, J. D., Green, C. M., & Fletcher, K. M. (2005). Revised gravity for offshore India and the isostatic compensation of submarine features. *Tectonophysics*, *404*(1–2), 1–22.

Becker, J. J., Sandwell, D. T., Smith, W. H. F., Braud, J., Binder, B., Depner, J., et al. (2009). Global bathymetry and elevation data at 30 arc seconds resolution: SRTM30_PLUS. *Marine Geodesy*, *32*(4), 355–371.

Bendat, J. S., & Piersol, A. G. (2010). *Random data: Analysis and measurement procedures, fourth edition*, Wiley Series in Probability and Statistics. Hoboken, NJ, USA: John Wiley.

Charette, M., & Smith, W. H. F. (2010). The volume of Earth's ocean. *Journal of The Oceanography Society*, *23*(2), 112–114.

Crough, S. T. (1978). Thermal origin of mid-plate hot-spot swells. *Geophysical Journal of the Royal Astronomical Society*, *55*, 451–469.

Dibarboure, G., Lamy, A., Pujol, M.-I., & Jettou, G. (2018). The drifting phase of SARAL: Securing stable ocean mesoscale sampling with an unmaintained decaying altitude. *Remote Sensing*, *10*(7), 1051.

Dixon, T. H., McNutt, M. K., & Smith, S. M. (1983). Bathymetric prediction from SEASAT altimeter. *Journal of Geophysical Research*, *88*(C3), 1563–1571.

Farr, T. G., Rosen, P. A., Caro, E., Crippen, R., Duren, R., Hensley, S., et al. (2007). The Shuttle Radar Topography Mission. *Reviews of Geophysics*, *45*, RG2004. https://doi.org/10.1029/2005RG000183

Ford, P. G., & Pettengill, G. H. (1992). Venus topography and kilometer-scale slopes. *Journal of Geophysical Research*, *97*(E8), 13,103–13,114.

Fu, L.-L., Alsdorf, D., Morrow, R., Rodriguez, E., & Mognard, N. (2012). SWOT: The Surface Water and Ocean Topography Mission wide-swath altimetric measurement of water elevation on Earth (*JPL 12-05*). Pasadena, CA.

GEBCO (2003). *Centenary edition of the GEBCO Digital Atlas, Intergovernmental Oceanographic Commission, International Hydrographic Organization, and British Oceanographic Data Centre*. Liverpool, U. K.: Br. Oceanogr. Data Cent.,.

GEBCO Bathymetric Compilation Group (2019). *The GEBCO_2019 Grid—A continuous terrain model of the global oceans and land*. UK: British Oceanographic Data Centre, National Oceanography Centre, NERC.

Garcia, E. S., Sandwell, D. T., & Smith, W. H. F. (2014). Retracking Cryosat-2, Envisat and Jason-1 radar altimetry waveforms for improved gravity field recovery. *Geophysical Journal International*, *196*(3), 1402–1422.

Gille, S. T. (1994). Mean sea surface height of the Antarctic Circumpolar Current from Geosat data: Method and application. *Journal of Geophysical Research*, *99*(C9), 18255.

Governments of Australia, M., & the People's Republic of China (2017). MH370 Phase 1 data.

Haxby, W. F., Karner, G. D., LaBrecque, J. L., & Weissel, J. K. (1983). Digital images of combined oceanic and continental data sets and their use in tectonic studies. *Eos, Transactions American Geophysical Union*, *64*(52), 995–1004.

Hess, H. H. (1962). History of ocean basins. In A. E. J. Engel, H. L. James, & B. Leonard (Eds.), *Petrologic studies: A volume to honor A F Buddington* (pp. 599–620). USA: The Geological Society of America.

Hochmuth, K., Gohl, K., & Uenzelmann-Neben, G. (2015). Playing jigsaw with large igneous provinces—A plate tectonic reconstruction of Ontong Java Nui, West Pacific. *Geochemistry Geophysics Geosystems*, *16*, 4449–4478. https://doi.org/10.1002/2015GC006036

Howat, I., Morin, P., Porter, C., & Noh, M.-J. (2018). The Reference Elevation Model of Antarctica. *The Cryosphere*, *13*, 665–674. Accessed from https://www.pgc.umn.edu/data/rema/ [12/27/2018].

IHO-IOC Commission (2018). *The IHO-IOC GEBCO cook book* (Vol. 103, pp. 416). Monaco: IHO Publication B-11. IOC Manuals and Guides 63, France, Sep. 2018, 429 pp.

JAMSTEC (2016). Japan Agency for Marine-Earth Science and Technology (2016) Data and Sample Research System for Whole Cruise Information in JAMSTEC (DARWIN).

Jakobsson, M., Mayer, L., Coakley, B., Dowdeswell, J. A., Forbes, S., Fridman, B., et al. (2012). The International Bathymetric Chart of the Arctic Ocean (IBCAO) Version 3.0. *Geophysical Research Letters*, *39*, L12609. https://doi.org/10.1029/2012GL052219

Jarvis, A., Reuter, H. I., Nelson, A., & Guevara, E. (2008). Hole-filled SRTM for the globe Version 4. Available from the CGIAR-CSI SRTM 90m database (http://srtm.csi.cgiar.org), 15, 25–54.

Koslow, J. A. (1997). Seamounts and the ecology of deep-sea fisheries. *American Scientist*, *85*(2), 168.

Kunze, E., & Llewellyn Smith, S. (2004). The role of small-scale topography in turbulent mixing of the global ocean. *Oceanography*, *17*(1), 55–64.

Lemoine, F. G., Smith, D. E., Kunz, L., Smith, R., Pavlis, E. C., Pavlis, N. K., et al. (1997). The development of the Joint NASA GSFC and the National Imagery and Mapping Agency (NIMA) Geopotential Model EGM96, *Gravity, geoid and marine geodesy* (pp. 461–469). Berlin, Heidelberg: Springer.

Markus, T., Neumann, T., Martino, A., Abdalati, W., Brunt, K., Csatho, B., et al. (2017). The Ice, Cloud, and land Elevation Satellite-2 (ICESat-2): Science requirements, concept, and implementation. *Remote Sensing of Environment*, *190*, 260–273.

Marty, J. C., & Cazenave, A. (1989). Regional variations in subsidence rate of oceanic plates: A global analysis. *Earth and Planetary Science Letters*, *94*(3-4), 301–315.

Matthews, K. J., Mller, R. D., Wessel, P., & Whittaker, J. M. (2011). The tectonic fabric of the ocean basins. *Journal of Geophysical Research*, *116*, B12109. https://doi.org/10.1029/2011JB008413

Mayer, L., Jakobsson, M., Allen, G., Dorschel, B., Falconer, R., Ferrini, V., et al. (2018). The Nippon Foundation GEBCO Seabed 2030 Project: The quest to see the world's oceans completely mapped by 2030. *Geosciences*, *8*(2), 63.

Mofjeld, H. O., Symons, C. M., Lonsdale, P., González, F. I., & Titov, V. V. (2004). Tsunami scattering and earthquake faults in the deep Pacific Ocean. *Oceanography*, *17*(1), 38–46.
Morrow, R., Church, J., Coleman, R., Chelton, D., & White, N. (1992). Eddy momentum flux and its contribution to the Southern Ocean momentum balance. *Nature*, *357*(6378), 482–484.
Müller, R. D., Roest, W. R., Royer, J.-Y., Gahagan, L. M., & Sclater, J. G. (1997). Digital isochrons of the world's ocean floor. *Journal of Geophysical Research*, *102*(B2), 3211–3214.
Müller, R. D., Sdrolias, M., Gaina, C., & Roest, W. R. (2008). Age, spreading rates, and spreading asymmetry of the world's ocean crust. *Geochemistry, Geophysics, Geosystems*, *9*, Q04006. https://doi.org/10.1029/2007GC001743
Müller, R. D., Seton, M., Watson, R. J., Qin, X., Williams, S., Zahirovic, S., et al. (2018). GPlates: Building a virtual earth through deep time. *Geochemistry, Geophysics, Geosystems*, *19*, 2243–2261. https://doi.org/10.1029/2018GC007584
Munk, W., & Wunsch, C. (1998). Abyssal recipes II: Energetics of tidal and wind mixing. *Deep Sea Research Part I: Oceanographic Research Papers*, *45*(12), 1977–2010.
Olson, C. J., Becker, J. J., & Sandwell, D. T. (2014). *A new global bathymetry map at 15 arcsecond resolution for resolving seafloor fabric: SRTM15_PLUS* (pp. OS34A–03). San Francisco: AGU Fall Meeting Abstracts.
Olson, CJ, Becker, JJ, & Sandwell, DT (2016). SRTM15_PLUS: Data fusion of Shuttle Radar Topography Mission (SRTM) land topography with measured and estimated seafloor topography (NCEI Accession 0150537).
Parsons, B. (1982). Causes and consequences of the relation between area and age of the ocean floor. *Journal of Geophysical Research*, *97*(B1), 289–302.
Parsons, B., & Sclater, J. G. (1977). An analysis of the variation of ocean floor bathymetry and heat flow with age. *Journal of Geophysical Research*, *82*(5), 803–827.
Picard, K., Brooke, B. P., Harris, P. T., Siwabessy, P. J. W., Coffin, M. F., Tran, M., et al. (2018). Malaysia Airlines flight MH370 search data reveal geomorphology and seafloor processes in the remote southeast Indian Ocean. *Marine Geology*, *395*(2017), 301–319.
Pitcher, T. J., Morato, T., Hart, P. J., Clark, M. R., Haggan, N., & Santos, R. S. (2008). Seamounts: Ecology, fisheries & conservation. Number October 2017.
Porter, C., Morin, P., Howat, I., Noh, M.-J., Bates, B., Peterman, K., et al. (2018). ArcticDEM. https://doi.org/10.7910/DVN/OHHUKH, Harvard Dataverse, V1, [10/29/2018].
Ramsayer, K. (2018). ICESat-2 reveals profile of ice sheets, sea ice, forests. NASA's Goddard Space Flight Center.
Ronov, A. B. (1994). Phanerozoic transgressions and regressions on the continents; a quantitative approach based on areas flooded by the sea and areas of marine and continental deposition. *American Journal of Science*, *294*(7), 777–801.
Royer, J. Y., & Sandwell, D. T. (1989). Evolution of the Eastern Indian Ocean since the Late Cretaceous: Constraints from geosataceous altimetry. *Journal of Geophysical Research*, *94*(B10), 13,755–13,782.
Sandwell, D., Garcia, E., Soofi, K., Wessel, P., Chandler, M., & Smith, W. H. F. (2013). Toward 1-mGal accuracy in global marine gravity from CryoSat-2, Envisat, and Jason-1. *The Leading Edge*, *32*(8), 892–899.
Sandwell, D. T., & Smith, W. H. F. (1997). Marine gravity anomaly from Geosat and ERS 1 satellite altimetry. *Journal of Geophysical Research*, *102*(B5), 10,039–10,054.
Sandwell, D. T., & Smith, W. H. F. (2001). Chapter 12 bathymetric estimation. *International Geophysics*, *69*(C), 441–457.
Sandwell, D. T., & Smith, W. H. (2005). Retracking ERS-1 altimeter waveforms for optimal gravity field recovery. *Geophysical Journal International*, *163*(1), 79–89.
Sandwell, D. T., & Smith, W. H. F. (2009). Global marine gravity from retracked Geosat and ERS-1 altimetry: Ridge segmentation versus spreading rate. *Journal of Geophysical Research*, *114*, B01411. https://doi.org/10.1029/2008JB006008
Sandwell, D. T., & Zhang, B. (1989). Global mesoscale variability from the Geosat Exact Repeat Mission: Correlation with ocean depth. *Journal of Geophysical Research*, *94*(C12), 17,971–17,984.
Sclater, J., Anderson, R. N., & Bell, M. L. (1971). Elevation of ridges and evolution of the central eastern Pacific. *Journal of Geophysical Research*, *76*(32), 7888–7915.
Sepulveda, I., Haase, J.S., Liu, P. L.-F., Grigoriu, M., Tozer, B., & Sandwell, D., (2019). Tsunami Hazard Assessment with Consideration of Uncertain Bathymetry. Asia Oceania Geophysical Society Conference. July 28th-August 2nd, Singapore.
Sepúlveda, I., Liu, P. L.-F., & Grigoriu, M. D. (2018). Probabilistic tsunami hazard assessment in South China Sea with consideration of uncertain earthquake characteristics. *Journal of Geophysical Research: Solid Earth*, *124*, 1–31. https://doi.org/10.1029/2018JB016620
Smith, W. H. F. (1998). Sea floor tectonic fabric. *Annual Review of Earth and Planetary Sciences*, *26*(1), 697–738.
Smith, W. H. (2015). Resolution of seamount geoid anomalies achieved by the SARAL/AltiKa and Envisat RA2 Satellite Radar Altimeters. *Marine Geodesy*, *38*, 644–671.
Smith, D. E., Head, J. W., Garvin, J. B., Banerdt, W. B., Muhleman, D. O., Pettengill, G. H., et al. (1999). The global topography of Mars and implications for surface evolution. *Science*, *284*(5419), 1495–1503.
Smith, W. H. F., & Marks, K. M. (2014). Sea floor in the Malaysia Airlines flight MH370 search area. *Eos*, *95*(21), 173–174.
Smith, W. H. F., & Sandwell, D. T. (1994). Bathymetric prediction from dense satellite altimetry and sparse shipboard bathymetry. *Journal of Geophysical Research*, *99*(B11), 21,803–21,824.
Smith, W. H. F., & Sandwell, D. T. (1997). Global sea floor topography from satellite altimetry and ship depth soundings. *Science*, *277*, 1956–1962.
Smith, W. H. F., & Wessel, P. (1990). Gridding with continuous curvature splines in tension. *Geophysics*, *55*(3), 293–305.
Smith, D. E., Zuber, M. T., Neumann, G. A., & Lemoine, F. G. (1997). Topography of the Moon from the Clementine lidar. *Journal of Geophysical Research*, *102*(E1), 1591–1611.
Stocker, T. F. (2013). *Ocean Circulation and Climate: Chapter 1. The ocean as a component of the climate system* (Vol. 103): Elsevier Inc. Chapters.
Tachikawa, T., Manabu, K., Iwasaki, A., Gesch, D., Oimoen, M., Zhang, Z., et al. (2011). ASTER global digital elevation model Version 2. Summary of Validation Results, page 7.
Watts, A. B., Sandwell, D. T., Smith, W. H. F., & Wessel, P. (2006). Global gravity, bathymetry, and the distribution of submarine volcanism through space and time. *Journal of Geophysical Research*, *111*, B08408. https://doi.org/10.1029/2005jb004083
Weatherall, P., Marks, K., Jakobsson, M., Schmitt, T., Tani, S., Arndt, J. E., et al. (2015). A new digital bathymetric model of the world's oceans. *Earth and Space Science*, *2*, 416–430.
Wessel, P. (2001). Global distribution of seamounts inferred from gridded Geosat/ERS-1 altimetry. *Journal of Geophysical Research*, *106*(B9), 19,431–19,441.
Wessel, P., & Smith, W. H. F. (1996). A global, self-consistent, hierarchical, high-resolution shoreline database. *Journal of Geophysical Research*, *101*(B4), 8741–8743.

Wessel, P., Smith, W. H. F., Scharroo, R., Luis, J., & Wobbe, F. (2013). Generic mapping tools: Improved version released. *Eos*, *94*(45), 409–410.

Willner, K., Shi, X., & Oberst, J. (2014). Phobos' shape and topography models. *Planetary and Space Science*, *102*(C), 51–59.

Wölfl, A.-C., Snaith, H., Amirebrahimi, S., Devey, C. W., Dorschel, B., Ferrini, V., et al. (2019). Seafloor mapping the challenge of a truly global ocean bathymetry. *Frontiers in Marine Science*, *6*, 283.

Zhang, S., Li, J., Jin, T., & Che, D. (2018). HY-2A altimeter data initial assessment and corresponding two-pass waveform retracker. *Remote Sensing*, *10*(4), 507.

Zhang, S., & Sandwell, D. T. (2017). Retracking of SARAL/AltiKa radar altimetry waveforms for optimal gravity field recovery. *Marine Geodesy*, *40*(1), 40–56.

Zitellini, N., Gràcia, E., Matias, L., Terrinha, P., Abreu, M. A., De Alteriis, G., et al. (2009). The quest for the Africa-Eurasia plate boundary west of the Strait of Gibraltar. *Earth and Planetary Science Letters*, *280*(1-4), 13–50.